Journal of Materials Chemistry A

Kinetic Processes of Phase Separation and Aggregation Behaviors in Slot-die Processed High Efficiency Y6-based Organic Solar Cells

Journal:	*Journal of Materials Chemistry A*
Manuscript ID	TA-ART-03-2022-002541.R1
Article Type:	Paper
Date Submitted by the Author:	12-May-2022
Complete List of Authors:	Xue, Jingwei; Xi'an Jiaotong University, State Key Laboratory for Mechanical Behavior of Materials Naveed, Hafiz Bilal; Xi'an Jiaotong University, State Key Laboratory for Mechanical Behavior of Materials Zhao, Heng; Xi'an Jiaotong University, State Key Laboratory for Mechanical Behavior of Materials Lin, Baojun; State Key Laboratory for Mechanical Behavior of Materials, Xi'an Jiaotong University, Xi'an 710049, China Wang, Yilin; Xi'an Jiaotong University Zhu, Qinglian; Xi'an Jiaotong University, State Key Laboratory for Mechanical Behavior of Materials Wu, Baohua; Xi'an Jiaotong University Bi, Zhaozhao; Xi'an Jiaotong University, b. State Key Laboratory for Mechanical Behavior of Materials Zhou, Xiaobo; Xian Jiaotong University Zhao, Chao; Xi'an Jiaotong University Zhou, Ke; Xi'an Jiaotong University, State Key Laboratory for Mechanical Behavior of Materials Ma, Wei; Xi'an Jiaotong University, State Key Laboratory for Mechanical Behavior of Materials

ARTICLE

Kinetic Processes of Phase Separation and Aggregation Behaviors in Slot-die Processed High Efficiency Y6-based Organic Solar Cells

Received 00th January 20xx,
Accepted 00th January 20xx

DOI: 10.1039/x0xx00000x

Jingwei Xue, ‡[a] Hafiz Bilal Naveed, ‡ [a] Heng Zhao,[a] Baojun Lin,[a] Yilin Wang,[a] Qinglian Zhu,[a] Baohua Wu,[a] Zhaozhao Bi,[a] Xiaobo Zhou,[a] Chao Zhao,[a] Ke Zhou*[a] and Wei Ma*[a]

The morphology optimization is proved to be one crucial factor contributing to the 19% efficient Y6-based organic solar cells (OSCs). Although the relationship between the component miscibility and film morphology has been established, it's not clarified how the film formation processes proceed, especially for the large-area fabrication compatible methods, i.e. slot-die coating, which obstacles the further optimization of morphology. Herein, we comprehensively investigated the effect of miscibility and film-formation kinetic process on the film morphology during the processing of different solvents. A highest power conversion efficiency (PCE) of 17.38% can be obtained in the D18:Y6 device processed with slot-die coating in an open-air environment. However, due to their relatively poor miscibility, incorporating trace amount of chlorobenzene (CB) into CF can sufficiently promote the Y6 aggregation, leading to the increased phase separation and thus the average PCE drop to 15.16%. On the contrary, PM6:Y6 blend shows the insensitive changes of kinetic process as well as final morphology and thus the comparable PCEs when cast with different solvents, which is ascribed to their relatively good miscibility. This work provides the scientific guidelines for device optimization by integrating the intermediate gap from miscibility to kinetic process and their impact on final morphology.

Introduction

Organic solar cells (OSCs) have a bright future due to their various advantages including flexibility, light weight, low cost, translucency, and large-area processing[1-6]. During recent years, researchers have put great efforts into the material design, morphology control, device engineering, and large-area fabrication of OSCs[7-14]. In particular, with the advent of sparkling non-fullerene acceptor Y6[10] and its derivatives, the power conversion efficiencies (PCEs) of OSCs have exceeded 19%, suggesting the great potential in practical application[13,14]. The emergence of Y6 and its derivatives have greatly contributed to the great prosperity of OSCs, achieving a breakthrough in efficiency and substantially accelerating the development of OSCs. Y6 employs a ladder-type electron-deficient-core-based central fused ring (dithienothiophen[3.2-b]-pyrrolobenzothiadiazole) with a benzothiadiazole (BT) core to fine-tune its absorption and electron affinity[10].The unique morphology that Y6 formed, such as 2D packing with a polymer-like conjugated backbone oriented normal to the substrate, is beneficial for improving carrier transport, which is conducive to the improvement of efficiency[15].

The morphology of active layer is one of the most critical factors in determining the device performance[16-25]. Typically, the solution-processed active layers feature a complex hierarchical structure, consisting of parameters with different length scale such as crystallinity, molecular orientation, domain size, and domain purity[26-28]. Small changes in material chemistry and process conditions can result in significant differences in morphology and the corresponding device performance[29,30]. The miscibility between donor and acceptor is a crucial thermodynamic factor reflecting the trend of phase separation during solution processing[31-33]. Different chemical species usually exhibit varied miscibility between the two materials, which tremendously affects their final morphology. For example, thermodynamic characterization indicates a room-temperature miscibility for D18:Y6 near the percolation threshold， which corresponds to an ideal quench depth and explains the near-ideal morphology for annealing using solvent vapor. In stark contrast, D18:IEICO-4Cl is a low-miscibility system with a deep quench depth during casting, which leads to poor morphology control and low performance[34]. Besides, the PDCBT-Cl:Y6 system with high miscibility results in a deficiency of phase separation, low domain purity, and poor crystallinity, and thus the poor PCE of

[a] State Key Laboratory for Mechanical Behavior of Materials, Xi'an Jiaotong University, Xi'an 710049, China. E-mail: msewma@xjtu.edu.cn; msekzhou@xjtu.edu.cn

Electronic Supplementary Information (ESI) available: [details of any supplementary information available should be included here]. See DOI: 10.1039/x0xx00000x

only 0.46%[32]. On the other hand, the alterations in film formation kinetics, which probably adjust the phase separation and aggregation behaviors of organic semiconductor materials, can affect the final morphology, even if the miscibility between the components remains unchanged[35-37]. For example, Liu et al. found that the PM6:Y6 system had completely different morphology and performances when processed with CF and CB[14]. The reason is due to the different arrangement structures of Y6, in which the face-on orientation in CF film and the low crystallinity and random crystal orientation in CB film can be observed. This leads to the decreased PCE in CB device. Lin et al. concluded that by matching the preaggregation rates between donor and acceptor during the film formation process with temperature-controlled slot-die coating, the optimized domain size and crystallinity can be achieved, which contributes to a PCE of 13.2% in PM7:IT4F[36]. As analyzed above, although the relationship between the component miscibility and film morphology has been established, it is not clarified how those phase separation and aggregation processes occur in the systems with different miscibility, which obstacles the understanding of morphology evolution mechanism and thus the further morphology optimization in those efficient blend systems.

In this paper, we select two high-efficiency systems to investigate the effect of miscibility and film-formation kinetic process on the film morphology during the processing of different solvents. In order to obtain the aggregation information and the spatial distribution of fluorophores and quencher within the blends during the solution-to-solid phase transformation, *in-situ* ultraviolet-visible (UV-vis) absorption and *in-situ* photoluminescence (PL) measurements were performed. We found that in the low miscibility D18[11]:Y6[10] system, the solution states of chloroform (CF) and mixed solvents (MS) (CF as the primary solvent with 0.5% v/v CB) are the same at the beginning of film formation. However, the solution concentration increases in the 0.5 s of film formation time while the strong interactions in chlorobenzene (CB) lead to enhanced aggregation and excessive phase separation and thus the deterioration of device performance. Therefore, the D18:Y6 exhibits the highest PCE of 17.38% in CF device due to the optimal morphology. In comparison, the average PCEs for MS and CB devices exhibit 15.16% and 13.44%, respectively. The film formation of the high-miscibility system PM6[38]:Y6 in CF and MS is analogous, leading to little variability in morphology and device performance. Therefore, the devices based on PM6:Y6 system obtain 14.70%, 14.23%, and 14.01% average efficiency when processed with CF, MS and CB, respectively. Our results suggest a powerful strategy for morphology optimization by considering both the miscibility and kinetic factors so as to control the phase separation and aggregation behaviors.

Results and discussion

Here, we chose two efficient blend systems D18:Y6 and PM6:Y6 to study the effect of miscibility and film-formation kinetic process on the film morphology and device performance. The chemical structures and energy levels of D18, PM6, and Y6 are displayed in Fig.1a and Fig.S1 (Supporting Information), respectively. The energy levels of D18:Y6 and PM6:Y6 are well aligned to split photon-generated excitons. The selection of the solvent is pivotal in the device preparation and has a direct association with the final morphology. Currently, the device processing in laboratories needs to select solvents by the trial-and-error method as so to achieve efficient devices. While the intrinsic reasons for the different morphology caused by different solvents should be further clarified. In our work, we chose the two most commonly used solvents, CF and CB, to adjust their blend film morphology. We firstly performed the contact angle measurements to study the interaction and miscibility among different components. The results are shown in Fig.S2 (Supporting Information). The interaction parameters, calculated according to Flory–Huggins model, are 0.64 for $\chi_{D18,\ Y6}$ and 0.58 for $\chi_{PM6,\ Y6}$, demonstrating better miscibility between PM6 and Y6 compared to that between D18 and Y6 (Fig.1b). To further investigate the interactions between polymers and Y6, we designed an experiment that used the *in-situ* temperature photoluminescence (PL) spectra of bilayer structure to verify the diffusion ability between polymers and Y6. As shown in Fig.S3 (Supporting Information), we prepared the structure with the lower layer as the donor D18 or PM6 and the upper layer as the acceptor Y6 to observe the change in the signal of Y6 under the effect of temperature. Time-dependent contour maps of PL spectra are shown in Fig.1c and 1d for PM6/Y6 and D18/Y6, respectively. The PL intensity of the bilayers of both systems is found to be reduced under the influence of temperature, as shown in Fig.1e. The bilayer absorbs photons to generate excitons under the light source, and the diffusion of excitons is intensified under the thermal effect, while the rapid quench of excitons is due to the presence of the donor-acceptor interface that causes the reduction of PL intensity. The donor-acceptor interface originates from two aspects, one is the original interface of the bilayer, and the other is the mixed region resulting from the rapid diffusion of Y6 into polymers upon thermal effect. In PM6/Y6, the intensity changed more strongly, while the signal changed relatively limited in the D18/Y6 system. The decrease in PL signal intensity may qualitatively respond to the diffusion of Y6 at the interface. Therefore, we qualitatively confirmed the better interdiffusion behavior between Y6 and PM6 from the above experiments, further suggesting their good miscibility.

To better understand the effect of CF and CB solvents on the morphology of active layer, a mixed solvent (MS) with the CF/CB blend ratio of 100/0.5 (V/V) was also employed to process the blend film so as to figure out the difference between CB and CF. The aggregation states of Y6 solutions and solid-state blend films were investigated by ultraviolet-visible (UV-vis) absorption spectroscopy. As shown in Fig.1f, the initial aggregation states of

Y6 in both CF and MS solvents are consistent, with the two lines coinciding exactly. In CB solvent, there is a slight overall blue shift of Y6 absorption peak, which proves its weaker aggregation state. The aggregation state of Y6 in the solid film is enhanced significantly compared to its solution state, and the peak position is significantly red-shifted. Fig.1g and 1h show the thin film absorption spectra of PM6:Y6 and D18:Y6 processed with different solvents. For D18:Y6, trace amount of CB made the peak position of Y6 significantly red-shifted (from 816 to 840 nm), close to the position of CB-processed film. While for PM6:Y6, trace amount of CB did not affect the peak position of Y6. This indicates the dramatically different aggregation of Y6 in two blend systems probably resulting from their various miscibility, we next studied how those different processing solvents affect the device performance and clarified the underlying mechanisms.

We prepared inverted devices with the structure of glass/ITO/ZnO/D18(PM6):Y6/MoO_3/Al using the slot-die coating in ambient conditions. Fig.2a shows the schematic of slot-die coating. The short-circuit current density-voltage (*J-V*) curves and the corresponding parameters are shown in Fig.2b and Table 1, respectively. In order to compare the PCE difference more intuitively, a histogram of the PCEs is illustrated in Fig.2c. D18:Y6 and PM6:Y6 are both high-efficiency systems, but their efficiency varies greatly when treated with different solvents. PM6:Y6 devices can obtain the high PCEs of around 14% processed with CF, MS and CB, which are not significantly affected by solvents. While only the D18:Y6 device cast with CF can obtain a high PCE of 17.38%, when treated with CB, the reduction in short-circuit current density (J_{SC}) and fill factor (FF) leads to a serious reduction in device performance. When using the MS, we found that the introduction of trace amount of CB had a significant effect on D18:Y6, while the efficiency of the PM6:Y6 system was slightly reduced in comparison. Fig.2d shows the external quantum efficiency (EQE) curves of the devices cast with different solvents. The current densities obtained from the EQE curves are consistent with those obtained from the *J-V* measurements.

Device physics processes including charge generation, transport and extraction were studied to explain the efficiency difference induced by the processing solvents. Firstly, the photocurrent density (J_{ph}) as a function of effective voltage (V_{eff}) was analyzed[39,40], where J_{ph} is defined as $J_{ph} = J_L - J_D$ (J_L and J_D are the current density under light illumination and in the dark, respectively) and V_{eff} is defined as $V_{eff} = V_0 - V_a$ (V_0 is the voltage at $J_{ph} = 0$ and V_a is the applied voltage). As shown in Fig.2e, for D18:Y6, the CF devices show higher J_{ph}/J_{sat} ratio (92.15%) than that of the MS (86.19%) and CB ones (78.57%) under short-circuit conditions, indicating the introduction of CB has affected charge extraction and carrier recombination. The exciton dissociation and charge extraction efficiency are more severely reduced in the CB-processed D18:Y6 device. The J_{ph}/J_{sat} ratios of CF, MS and CB in the PM6:Y6 system are 91.63%, 91.28% and 87.32%, respectively, indicating that the CF device has the most efficient dissociation efficiency and while it is slightly reduced in the MS device. In addition, the carrier recombination mechanism was studied by measuring the dependence of J_{SC} and V_{OC} under varied illumination intensity. Generally, the dependence of J_{SC} on light intensity (*P*) can be used to characterize the bimolecular recombination. J_{SC} is proportional to P^{α}, where α is the power-law exponent that can be extracted from fitting the slope of the data plotted on a log-log scale[41,42]. The relationship between V_{OC} and *P* can be used to distinguish whether bimolecular recombination (slope of kT/q, where *k* is Boltzmann's constant and T represents the absolute temperature) or trap-assisted recombination (2 kT/q) dominants the recombination mechanism[42,43]. As shown in Fig.2f and 2g, for D18:Y6, the α values of CF, MS and CB devices are 0.927, 0.918 and 0.907, respectively, indicating lower bimolecular recombination of CF devices. While in PM6:Y6 system, the α values of CF, MS and CB devices are 0.951, 0.937 and 0.927, respectively, exhibiting a similar trend to D18:Y6 system. Besides, for D18:Y6 and PM6:Y6, the CF devices show a small slope of 1.17 kT/q and 1.28 kT/q, while the CB devices show a large slope of 1.45 kT/q and 1.37 kT/q, suggesting the weak trap-assisted recombination of CF devices. For D18:Y6/MS device, the introduction of CB leads to an increase in bimolecular recombination and trap-assisted recombination, resulting in a gradual decrease in device performance. The introduction of CB in PM6:Y6 system has merely effect on the trap-assisted recombination since the CF and MS devices have the same slope of 1.28kT/q. Moreover, the hole mobility (μ_h) and electron mobility (μ_e) were measured under different conditions using space-charge-limited current (SCLC) method. As shown in Fig.2h and Fig.2i, for D18:Y6 system, both μ_h and μ_e have higher values and the μ_h / μ_e ratio is more balanced in CF device. However, the values of μ_h and μ_e are severely reduced and out of balance in MS devices. The values of μ_e are calculated to be 4.14×10^{-4} and 3.01×10^{-4} $cm^2 V^{-1} s^{-1}$ for the CF and MS devices, respectively, while the μ_h values of the corresponding devices are 4.58×10^{-4} and 4.09×10^{-4} $cm^2 V^{-1} s^{-1}$. The weakened and unbalanced charge carrier motions indicate the unfavorable competition between charge recombination and charge generation, which further affects the FF values. In PM6:Y6 system, the values of μ_e were calculated to be 3.42×10^{-4} and 3.38×10^{-4} $cm^2 V^{-1} s^{-1}$ for the CF and MS devices, respectively, and the μ_h values of the corresponding devices were 3.71×10^{-4} and 3.60×10^{-4} $cm^2 V^{-1} s^{-1}$. The values of μ_h and μ_e are weakly reduced when changing the processing solvent from CF to MS, therefore the FF values are maintained.

The performance of OSCs is directly related to the morphology of active layer. Therefore, the grazing-incidence wide-angle X-ray scattering (GIWAXS)[44] measurement was used to study the molecular packing and crystallinity in D18:Y6 and PM6:Y6 films prepared by slot-die coating with different solvents. Fig.3a-b and Fig.3c show the 2D-GIWAXS images and the corresponding line profiles of D18:Y6 and PM6:Y6 blend films. All blends exhibit face-on preferential orientation. In addition, to quantify the molecular crystallinity, the crystalline coherence length (CCL), which is

closely related to the charge transport and device performance, is extracted from GIWAXS line profiles according to Scherrer equation[45], as summarized in Table 2. With the incorporation of CB, the D18:Y6 blend shows sharper (100) lamellar packing (q = 0.29 Å^{-1}), while the PM6:Y6 blend shows no significant change in (100) lamellar packing (q = 0.28 Å^{-1}), indicating the strong effect of CB on the D18 alignment and the limited effect on PM6 film. For D18:Y6 film the CCL of MS blends (99.66 Å) is higher than that of the CF film (94.27 Å). While the CCL of MS blends (69.98 Å) is only slightly improved than that of the CF blends (69.39 Å) in PM6:Y6. For CB films, the (100) peaks of both systems are greatly enhanced compared to CF films with CCL enhanced from 94.27 Å and 69.39 Å to 151.9 Å and 95.64 Å for D18:Y6 and PM6:Y6 systems, respectively. The CCL of D18 is increased by 6% and 61% in MS and CB films, respectively, compared to CF film, which corresponds to a decrease in PCE from 17.1% to 15.3% and 13.4%. By comparing the changes in the arrangement of the two donors, we can observe that the effect of trace amount of CB on the crystallinity of D18 and PM6 is different. Trace amount of CB has a profound effect on the behavior of D18, while the arrangement of PM6 remains almost unchanged in comparison.

Then we performed resonant soft X-ray scattering (RSoXS)[46] to further probe the phase separation in different conditions. We used 286.8 and 284.2 eV X-ray to gain high scattering contrast on D18:Y6 and PM6:Y6 blend films, respectively, and Fig.3d and 3e show the RSoXS line profiles. The phase separation parameters are extracted and summarized in Table S2. Impressively, for D18:Y6, the CF and MS blend films show the scattering peaks at q = 0.181 and 0.157 nm^{-1}, respectively, exhibiting a much larger domain size of MS film (23.84 nm) than that of CF film (17.32 nm). However, the domain size is only weakly enhanced from CF (32.98 nm) to MS (33.90 nm) in PM6:Y6 films. The trace CB has a profound effect on the morphology of D18:Y6. In addition, we also investigated the morphology of the active layer using atomic force microscopy (AFM) and transmission electron microscopy (TEM). For D18:Y6 system, as shown in Fig.S6a-b, the surface morphology of the CF film is relatively smooth, with an average mean square surface roughness (R_q) of 1.26 nm and an obvious fibrous structure in the corresponding phase diagram. However, when processed with CB, the surface roughness increases significantly with R_q of 3.72 nm, which may have a negative impact on charge generation and collection. As a result, the relatively poor J_{SC} and FF values are observed in the CB-processed D18:Y6 devices. TEM images also show that D18:Y6 films have a highly regular arrangement structure when processed with CB, which exhibits a significantly larger phase separation as well as a large enhancement of the D18 arrangement regularity (Fig.S6e-f). In contrast, in the PM6:Y6 system, the surface roughness of the film increases slightly when processed with CB compared to CF, with the average R_q increasing from 1.44 to 1.56 nm (Fig.S6c-d), which corresponds well to a limited increase in the size of TEM phase region (Fig.S6g-h), and thus the nearly unchanged device performance. Therefore, D18 in the D18:Y6 system exhibits strong aggregation behavior when processed with CB, resulting in a dramatic increase in crystallinity and phase separation, which severely affects the exciton dissociation and charge extraction processes.

In order to gain a deeper understanding of the morphology evolution during film drying in slot-die coating under different conditions, *in-situ* spectroscopy measurements were performed. Fig.4a-c and 4e-g show the time evolution of UV-vis absorption contour maps of D16 and PM6:Y6 films in different solvents, where the raw *in-situ* UV-vis absorption spectra are shown in Fig.S7. The UV-vis absorption spectra are calculated from the transmission spectra according to the equation $A_\lambda = -\log_{10}(T)$, where A_λ is the absorbance at a certain wavelength (λ) and T is the measured transmittance after background correction using blank glass[47]. Fig.S8a-c and Fig.S8e-f show the time evolution of photoluminescence (PL) contour maps of D18:Y6 and PM6:Y6 films in different solvents, where the raw data are shown in Fig.S9. Fig.4d and 4h show the time evolution of Y6 peak location extracted from *in-situ* UV-vis absorption in D18:Y6 and PM6:Y6 films, respectively. The evolution of peak location represents the aggregation behavior of donor and acceptor. Fig.S8d and S8h show the time evolution of integral PL intensity, which can be correlated to the spatial distribution of fluorophores and quencher within the blends[48]. Y6 peak evolution can be divided into three stages: 1) during the first stage, as the solvent evaporates, Y6 absorption peaks do not evolve, while its integral PL intensity reduces slowly at the beginning and then decreases rapidly due to the increased solution concentration. The reduction of integral PL intensity indicates that the average distance between the homogenously distributed fluorophores and quencher decreases as the relative concentration increases. Moreover, CB takes the longest time to complete this process from the view of time scale, while the time for MS is slightly longer than that of CF. 2) During the second stage, as the solvent continuously evaporates, the solution concentration crosses the solubility limit and reaches critical supersaturation. Under such extreme supersaturation, the absorption peak location of Y6 starts to red shift, while the integral PL intensity further decreases, indicating the onset of Y6 aggregation. As shown in Fig.4d and 4h, the redshift onset of Y6 peak location in CF blend happens earlier than that in MS blend, indicating that Y6 molecules aggregate in advance with the incorporation of CB. 3) As the solvent further evaporates, Y6 absorption peak exhibits the continuously red shift and then stabilizes when all the solvents are removed at the third stage. By comparing the signal changes, we found that the Y6 signal in the two systems had a dramatic difference after the solvents change. We found an interesting phenomenon that the introduction of trace amount of CB could cause a significant red shift of Y6 peak position in D18:Y6 system, and the final state of Y6 in MS is consistent with that in CB, indicating the significant aggregation. However, we did not find this phenomenon in PM6:Y6 system, and the introduction of CB did not have an obvious effect on Y6 aggregation. The

aggregation behavior of Y6 in the mixture solvent is much closer to that in CF. Therefore, Y6 in the D18:Y6 system is strongly affected by trace CB. For D18:Y6 system, the trace CB changed the aggregation and the position of the final absorption peak of Y6 due to the increased film drying time combined with the poor miscibility between D18 and Y6, which leads to the excessive phase separation size and crystallinity of D18 in the film.

On the basis of all the results discussed above, we have gained a whole picture (Fig.5) of how trace CB enables the aggregation of Y6 in D18:Y6 and PM6:Y6 systems. In the solution state, trace amount of CB has not affected the aggregation states of Y6 in two systems. During the film formation process, the total concentration increases with the solvent evaporation, and the Y6 aggregation in D18:Y6 system becomes more obvious (Fig.4d) due to the poor miscibility between D18 and Y6 and the extended molecular diffusion time facilitated by the residual CB solvent (~ 0.5 s), resulting in excessive aggregation in D18:Y6 blend. With further evaporation of the solvent, the domains of D18 and Y6 grow rapidly based on the aggregates already assembled, promoting the formation of ordered structures. As a result, the over-crystallization of D18 and the excessive growth of phase separation can be obtained. However, in PM6:Y6 system, the aggregation state is not affected by trace CB and remains the same as that in CF. Thus, the final phase separation and the crystallization of PM6 are maintained.

Conclusions

In summary, we have comprehensively investigated the effect of miscibility and film-formation kinetic process on the film morphology during the processing with different solvents. We found that in the low miscibility D18:Y6 system, trace amount of CB causes a significant aggregation of Y6. The solution concentration increases in the 0.5 s of film formation time while the strong interactions in CB lead to enhanced aggregation and excessive phase separation. Thus, the D18:Y6 exhibits the highest PCE of 17.38% in CF devices due to the optimal morphology, while the MS device exhibits only an average PCE of 15.16%. In comparison, the film formation of the high-miscibility system PM6:Y6 in CF and MS is analogous, which results in little variability in morphology and the corresponding device performance. This work has clarified the underlying mechanism for the device optimization by connecting the relationships among component miscibility, film-formation kinetic process, and final morphology, which paves the way to further improve the device performance in solution-processed OSCs.

Author contribution statement

JX and HN contribute equally to this work. JX fabricated the solar cell devices and performed the UV, PL, AFM; HN made an important contribution by completing the experiments and data processing required for review comments during the laboratory closure due to the Covid-19; HZ and BL analyzed the RSoXS data; YW, QZ and BW analyzed the GIWAXS data; ZB, XZ and CZ helped in the data interpretation; WM and KZ conceived and directed the experiment. All authors contributed to analysis and manuscript writing.

Conflicts of interest

There are no conflicts to declare.

Acknowledgements

Thanks for the support from NSFC (52173023, 21875182), Key Scientific and Technological Innovation Team Project of Shaanxi Province (2020TD-002), and 111 project 2.0 (BP2018008). X-ray data was acquired at beamlines 7.3.3 and 11.0.1.2 at the Advanced Light Source, which is supported by the Director, Office of Science, Office of Basic Energy Sciences, of the U.S. Department of Energy under Contract No. DE-AC02-05CH11231. The authors thank Chenhui Zhu at beamline 7.3.3, and Cheng Wang at beamline 11.0.1.2 for assistance with data acquisition.

References

1. F. . W. N . S . Sariciftci , L . Smilowitz , A . J . Heeger, *Science*, 2009, **258**, 1474–1476.
2. G. Yu, J. Gao, J. C. Hummelen, F. Wudl and A. J. Heeger, *Science*, 1995, **270**, 1789–1791.
3. J. L. O'Brien, A. Furusawa and J. Vučković, *Nat. Photonics*, 2009, **3**, 687–695.
4. G. Li, R. Zhu and Y. Yang, *Nat. Photonics*, 2012, **6**, 153–161.
5. A. J. Heeger, *Adv. Mater.*, 2014, **26**, 10–28.
6. Z. Zhou, S. Xu, J. Song, Y. Jin, Q. Yue, Y. Qian, F. Liu, F. Zhang and X. Zhu, *Nat. Energy*, 2018, **3**, 952–959.
7. Y. Lin, J. Wang, Z. G. Zhang, H. Bai, Y. Li, D. Zhu and X. Zhan, *Adv. Mater.*, 2015, **27**, 1170–1174.
8. J. Wang and X. Zhan, *Acc. Chem. Res.*, 2021, **54**, 132–143.
9. S. Zhang, Y. Qin, J. Zhu and J. Hou, *Adv. Mater.*, 2018, **30**, 1800868.
10. J. Yuan, Y. Zhang, L. Zhou, G. Zhang, H. L. Yip, T. K. Lau, X. Lu, C. Zhu, H. Peng, P. A. Johnson, M. Leclerc, Y. Cao, J. Ulanski, Y. Li and Y. Zou, *Joule*, 2019, **3**, 1140–1151.
11. Q. Liu, Y. Jiang, K. Jin, J. Qin, J. Xu, W. Li, J. Xiong, J. Liu, Z. Xiao, K. Sun, S. Yang, X. Zhang and L. Ding, *Sci. Bull.*, 2020, **65**, 272–275.
12. C. Li, J. Zhou, J. Song, J. Xu, H. Zhang, X. Zhang, J. Guo, L. Zhu, D. Wei, G. Han, J. Min, Y. Zhang, Z. Xie, Y. Yi, H. Yan, F. Gao, F. Liu and Y. Sun, *Nat. Energy*, 2021, **6**, 605–613.
13. Y. Cui, Y. Xu, H. Yao, P. Bi, L. Hong, J. Zhang, Y. Zu, T. Zhang, J. Qin, J. Ren, Z. Chen, C. He, X. Hao, Z. Wei and J. Hou, *Adv.*

Mater., 2021, **33**, 2102420.
14. K. Chong, X. Xu, H. Meng, J. Xue, L. Yu, W. Ma and Q. Peng, *Adv. Mater.*, 2022, 2109516.
15. L. Zhu, M. Zhang, G. Zhou, T. Hao, J. Xu, J. Wang, C. Qiu, N. Prine, J. Ali, W. Feng, X. Gu, Z. Ma, Z. Tang, H. Zhu, L. Ying, Y. Zhang and F. Liu, *Adv. Energy Mater.*, 2020, **10**, 1904234.
16. M. Zhang, F. Zhang, Q. An, Q. Sun, W. Wang, X. Ma, J. Zhang and W. Tang, *J. Mater. Chem. A*, 2017, **5**, 3589–3598.
17. H. Lee, C. Park, D. H. Sin, J. H. Park and K. Cho, *Adv. Mater.*, 2018, **30**, 1800453.
18. F. Zhao, C. Wang and X. Zhan, *Adv. Energy Mater.*, 2018, **8**, 1703147.
19. C. McDowell, M. Abdelsamie, M. F. Toney and G. C. Bazan, *Adv. Mater.*, 2018, **30**, 1707114.
20. S. Zhang, L. Ye, H. Zhang and J. Hou, *Mater. Today*, 2016, **19**, 533–543.
21. E. F. Manley, J. Strzalka, T. J. Fauvell, N. E. Jackson, M. J. Leonardi, N. D. Eastham, T. J. Marks and L. X. Chen, *Adv. Mater.*, 2017, **29**, 1703933.
22. E. F. Manley, J. Strzalka, T. J. Fauvell, T. J. Marks and L. X. Chen, *Adv. Energy Mater.*, 2018, **8**, 1800611.
23. K. Gao, L. Li, T. Lai, L. Xiao, Y. Huang, F. Huang, J. Peng, Y. Cao, F. Liu, T. P. Russell, R. A. J. Janssen and X. Peng, *J. Am. Chem. Soc.*, 2015, **137**, 7282–7285.
24. K. Gao, J. Miao, L. Xiao, W. Deng, Y. Kan, T. Liang, C. Wang, F. Huang, J. Peng, Y. Cao, F. Liu, T. P. Russell, H. Wu and X. Peng, *Adv. Mater.*, 2016, **28**, 4727–4733.
25. K. Gao, W. Deng, L. Xiao, Q. Hu, Y. Kan, X. Chen, C. Wang, F. Huang, J. Peng, H. Wu, X. Peng, Y. Cao, T. P. Russell and F. Liu, *Nano Energy*, 2016, **30**, 639–648.
26. F. Liu, Y. Gu, X. Shen, S. Ferdous, H. W. Wang and T. P. Russell, *Prog. Polym. Sci.*, 2013, **38**, 1990–2052.
27. F. Liu, Y. Gu, J. W. Jung, W. H. Jo and T. P. Russell, *J. Polym. Sci. Part B Polym. Phys.*, 2012, **50**, 1018–1044.
28. J. R. Tumbleston, B. A. Collins, L. Yang, A. C. Stuart, E. Gann, W. Ma, W. You and H. Ade, *Nat. Photonics*, 2014, **8**, 385–391.
29. Z. Li, K. Jiang, G. Yang, J. Y. L. Lai, T. Ma, J. Zhao, W. Ma and H. Yan, *Nat. Commun.*, 2016, **7**, 13094.
30. Y. Liu, J. Zhao, Z. Li, C. Mu, W. Ma, H. Hu, K. Jiang, H. Lin, H. Ade and H. Yan, *Nat. Commun.*, 2014, **5**, 5293.
31. L. Ye, H. Hu, M. Ghasemi, T. Wang, B. A. Collins, J. H. Kim, K. Jiang, J. H. Carpenter, H. Li, Z. Li, T. McAfee, J. Zhao, X. Chen, J. L. Y. Lai, T. Ma, J. L. Bredas, H. Yan and H. Ade, *Nat. Mater.*, 2018, **17**, 253–260.
32. Z. Liang, M. Li, Q. Wang, Y. Qin, S. J. Stuard, Z. Peng, Y. Deng, H. Ade, L. Ye and Y. Geng, *Joule*, 2020, **4**, 1278–1295.
33. M. Gao, Z. Liang, Y. Geng and L. Ye, *Chem. Commun.*, 2020, **56**, 12463–12478.
34. Z. Wang, Z. Peng, Z. Xiao, D. Seyitliyev, K. Gundogdu, L. Ding and H. Ade, *Adv. Mater.*, 2020, **32**, 2005386.
35. Z. Wang, K. Gao, Y. Kan, M. Zhang, C. Qiu, L. Zhu, Z. Zhao, X. Peng, W. Feng, Z. Qian, X. Gu, A. K. Y. Jen, B. Z. Tang, Y. Cao, Y. Zhang and F. Liu, *Nat. Commun.*, 2021, **12**, 332.
36. B. Lin, X. Zhou, H. Zhao, J. Yuan, K. Zhou, K. Chen, H. Wu, R. Guo, M. A. Scheel, A. Chumakov, S. V. Roth, Y. Mao, L. Wang, Z. Tang, P. Müller-Buschbaum and W. Ma, *Energy Environ. Sci.*, 2020, **13**, 2467–2479.
37. H. Zhao, H. B. Naveed, B. Lin, X. Zhou, J. Yuan, K. Zhou, H. Wu, R. Guo, M. A. Scheel, A. Chumakov, S. V. Roth, Z. Tang, P. Müller-Buschbaum and W. Ma, *Adv. Mater.*, 2020, **32**, 2002302.
38. M. Zhang, X. Guo, W. Ma, H. Ade and J. Hou, *Adv. Mater.*, 2015, **27**, 4655–4660.
39. M. Lenes, M. Morana, C. J. Brabec and P. W. M. Blom, *Adv. Funct. Mater.*, 2009, **19**, 1106–1111.
40. V. D. Mihailetchi, L. J. A. Koster, J. C. Hummelen and P. W. M. Blom, *Phys. Rev. Lett.*, 2004, **93**, 19–22.
41. C. M. Proctor, M. Kuik and T. Q. Nguyen, *Prog. Polym. Sci.*, 2013, **38**, 1941–1960.
42. S. R. Cowan, A. Roy and A. J. Heeger, *Phys. Rev. B*, 2010, **82**, 245207.
43. A. K. K. Kyaw, D. H. Wang, V. Gupta, W. L. Leong, L. Ke, G. C. Bazan and A. J. Heeger, *ACS Nano*, 2013, **7**, 4569–4577.
44. A. Hexemer, W. Bras, J. Glossinger, E. Schaible, E. Gann, R. Kirian, A. MacDowell, M. Church, B. Rude and H. Padmore, *J. Phys. Conf. Ser.*, 2010, **247**, 012007.
45. D. M. Smilgies, *J. Appl. Crystallogr.*, 2009, **42**, 1030–1034.
46. E. Gann, A. T. Young, B. A. Collins, H. Yan, J. Nasiatka, H. A. Padmore, H. Ade, A. Hexemer and C. Wang, *Rev. Sci. Instrum.*, 2012, **83**, 045110.
47. M. Abdelsamie, K. Zhao, M. R. Niazi, K. W. Chou and A. Amassian, *J. Mater. Chem. C*, 2014, **2**, 3373–3381.
48. S. Engmann, F. A. Bokel, H. W. Ro, D. M. DeLongchamp and L. J. Richter, *Adv. Energy Mater.*, 2016, **6**, 1502011.

ARTICLE

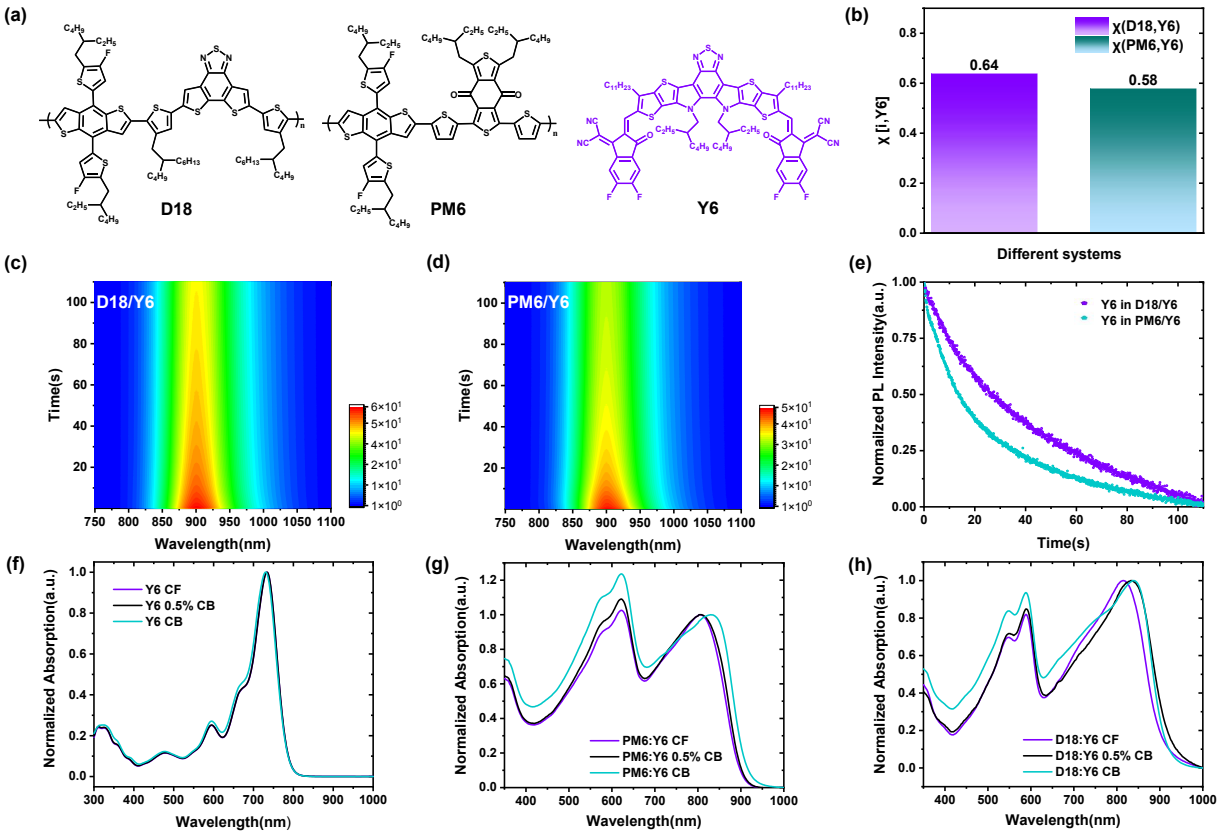

Fig. 1. (a) The Chemical structure of D18, PM6 and L8-BO. (b) The interaction parameters for PM6: Y6 and D18:Y6. Time-dependent contour maps of PL spectra for (c) D18/Y6 and (d) PM6/Y6. (e) Time evolution of normalized PL intensity of D18/Y6 and PM6/Y6. The ultraviolet–visible (UV–vis) absorption of (f) Y6 solutions and blend solid film for (g) PM6: Y6 and (h) D18:Y6.

ARTICLE

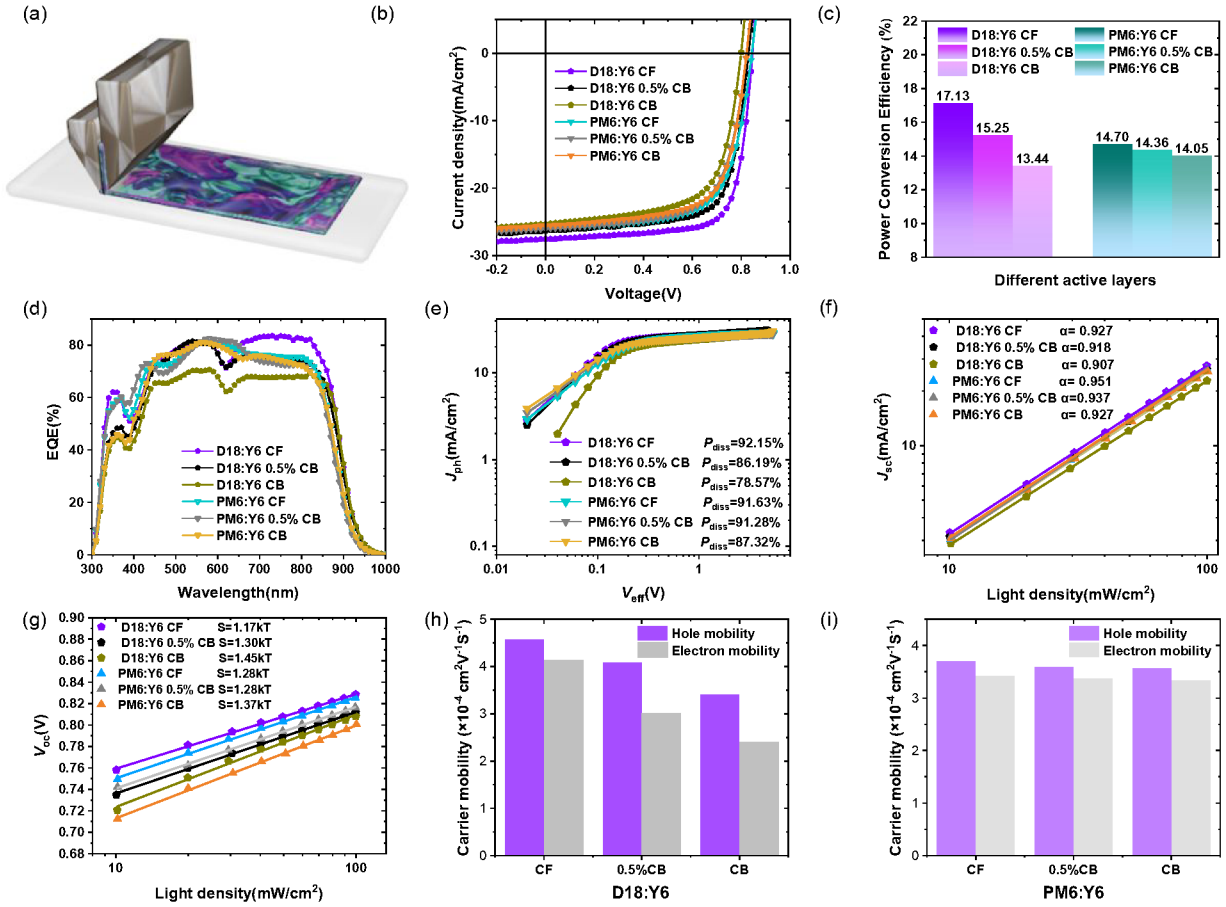

Fig. 2. (a) Schematic illustration of slot-die coating. The (b) *J*-*V* curves, (c) power conversion efficiency (PCE) comparison histogram, (d) EQE curves, (e) J_{ph}-V_{eff} curves, the dependence of (f) short-circuit current density and (g) open-circuit voltage on light intensity, and (h, i) charge carrier mobility histogram of D18:Y6 and PM6:Y6 with different solvents.

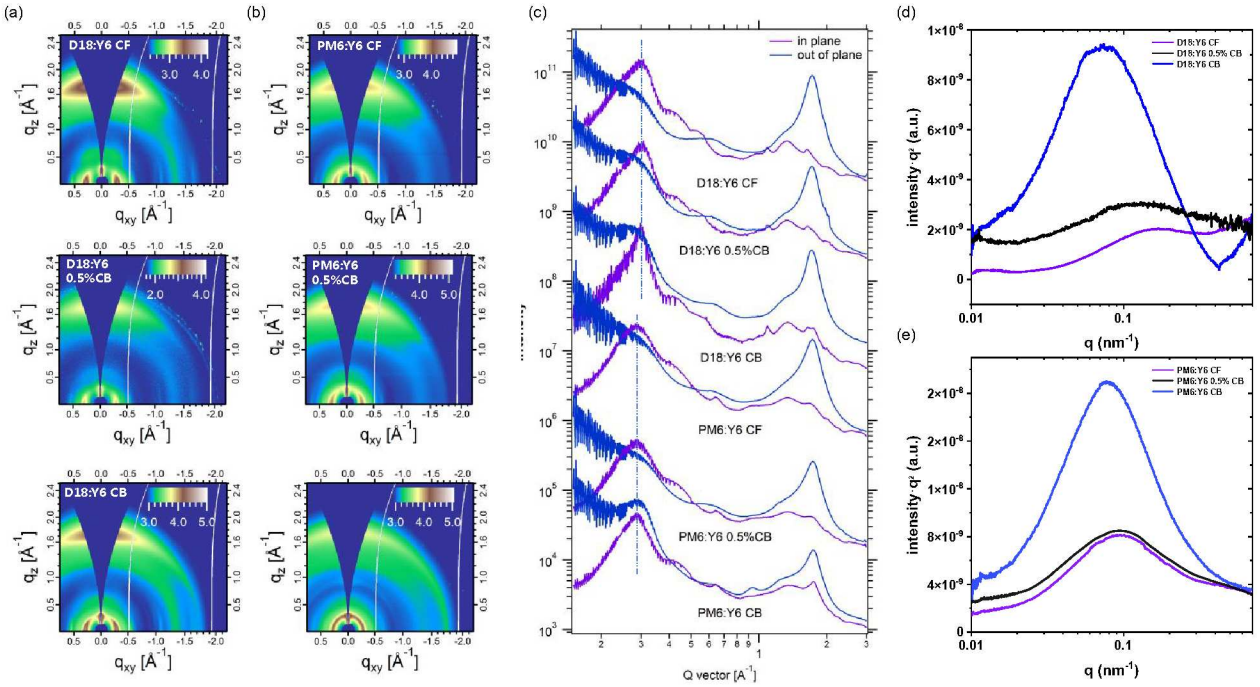

Fig. 3. GIWAXS (a-b) 2D patterns, (c) line profiles and RSoXS profiles of (d) D18:Y6 and (e) PM6:Y6 blend films with different solvents.

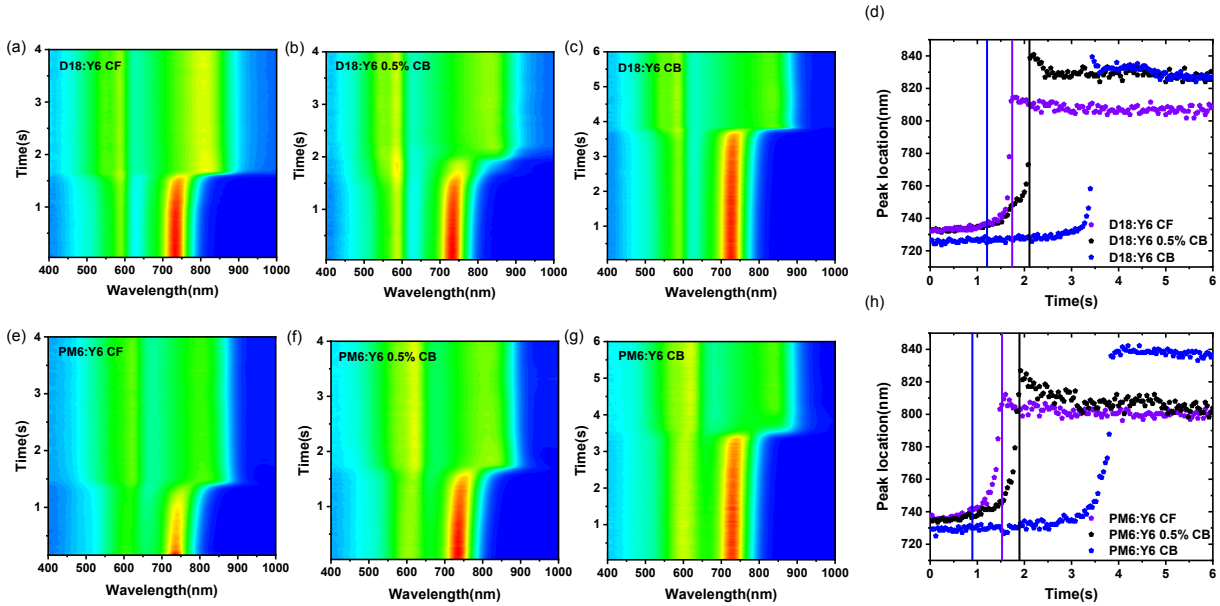

Fig. 4. Time-dependent contour maps of UV-vis absorption spectra for (a-c) D18:Y6 and (e-g) PM6:Y6 during slot-die coating with different solvent. Time evolution of peak location of Y6 for (d) D18:Y6 and (h) PM6:Y6 during slot-die coating with different solvents. The blue line indicates the onset, and the purple and black lines indicate the stop times for CF and 0.5%CB conditions.

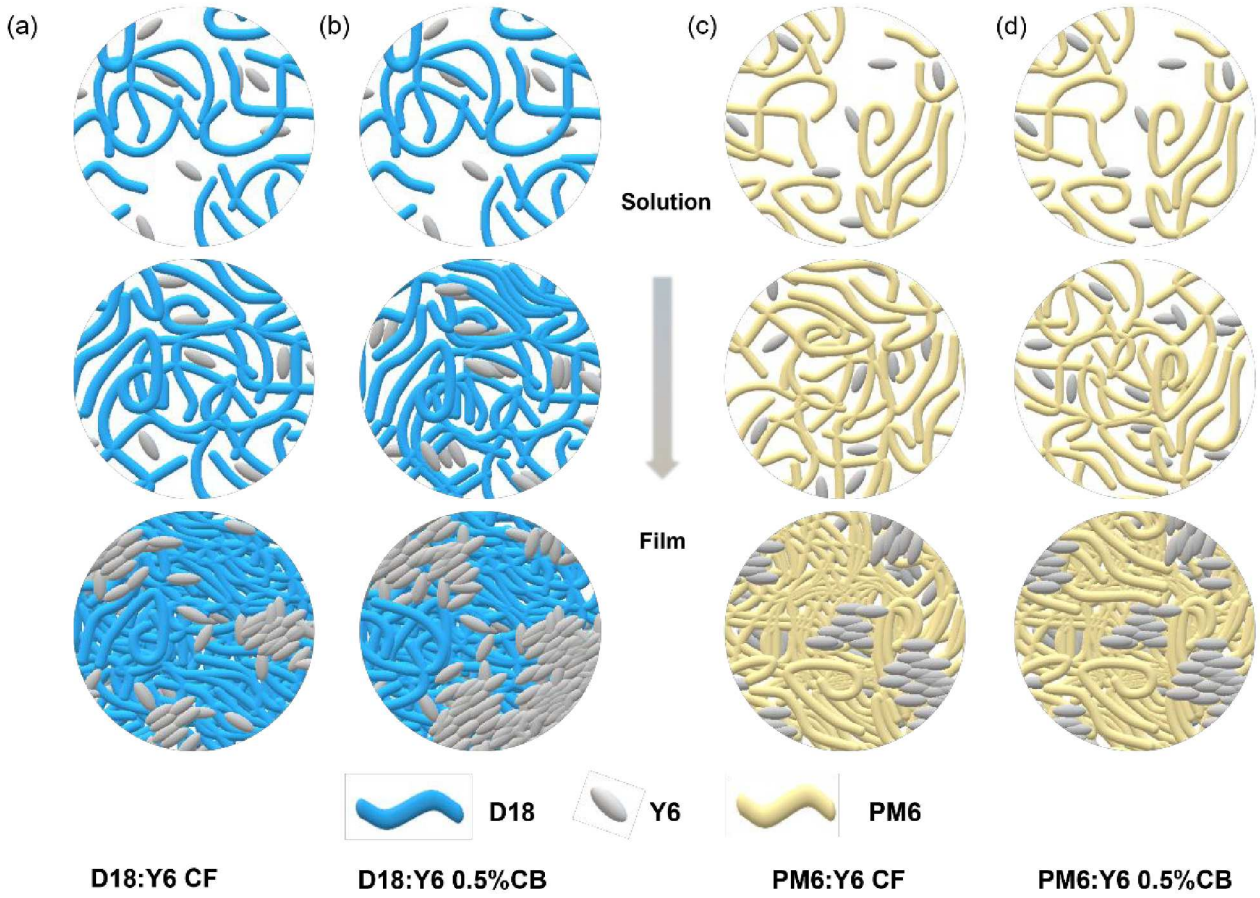

Fig. 5. Schematic diagram of the aggregation status in solution and film for D18:Y6 (a, b) and PM6:Y6 (c, d) processed by CF and MS.

Table 1. Photovoltaic parameters of OSCs with different active layer under the illumination of AM 1.5G, 100 mW cm^{-2} (The average PCEs are obtained from at least 10 devices).

Active layer	Solvent	V_{OC} [V]	J_{SC} [mA/cm^2]	FF [%]	PCE [%]	PCE_{max} [%]
D18:Y6	CF	0.844 ± 0.002	27.37 ± 0.17	73.91 ± 0.44	17.13 ± 0.13	17.38
	0.5%CB	0.826 ± 0.004	26.07 ± 0.39	70.28 ± 0.66	15.16 ± 0.12	15.42
	CB	0.818 ± 0.005	24.00 ± 0.29	68.64 ± 0.55	13.44 ± 0.16	13.67
PM6:Y6	CF	0.841 ± 0.004	25.70 ± 0.24	68.04 ± 0.88	14.70 ± 0.15	15.03
	0.5%CB	0.824 ± 0.006	25.66 ± 0.44	67.44 ± 0.98	14.23 ± 0.18	14.72
	CB	0.820 ± 0.008	25.24 ± 0.49	67.44 ± 0.86	14.01 ± 0.13	14.29

Table 2. The Structure Parameters of D18:Y6 and PM6:Y6 blend active layers with different solvents for (100) peak obtained from GIWAXS data.

	solvent	location [$Å^{-1}$]	d-spacing [$Å^{-1}$]	FWHM	CCL [Å]
D18:Y6	CF	0.293	21.44	0.060	94.27
	0.5%CB	0.298	21.11	0.057	99.66
	CB	0.297	21.16	0.037	151.9
PM6:Y6	CF	0.283	22.22	0.081	69.39
	0.5%CB	0.283	22.20	0.081	69.98
	CB	0.297	21.16	0.059	95.64